Multiscale Computation of Cytoskeletal Mechanics During Blebbing

Sorin Mitran and Jennifer Young

Abstract Cellular blebbing occurs when detachment of the underlying cytoskeleton from a portion of the plasma membrane leads to the formation of protrusions under the influence of cytosol pressure. Blebbing is associated with cellular apoptosis and has been linked to diseased states such as cancer. Multiple phenomena at disparate scales occur during blebbing. At the molecular scale there are biochemical reactions governing actin polymerization, cross-linkage, and formation of membrane adhesion complexes. At the cellular level, forces on the cell membrane lead to deformation of the cytoskeleton and localized mechanical stress. Fluid motion during protrusive activity modifies local concentrations of free actin monomers as well as other molecules that participate in cytoskeleton formation. A computational model of cellular blebbing has to link these disparate scales. In this work a general multiscale interaction procedure is applied to the problem of cellular blebbing. The procedure simultaneously advances in time three models of the cytoskeleton at three different length scales. At the smallest length scale the Langevin dynamics of small actin filament segments is computed by solving stochastic differential equations. At larger scales the cytoskeleton actin network is characterized by probability distribution functions for parameters such as actin filament length and orientation. A Fokker–Planck equation is formulated for the probability distribution functions and advanced in time. At an even larger scale the cytoskeleton is modeled as a continuum, and inhomogeneous elasticity equations are solved. The overall procedure is efficient enough to show cellular level effects produced by changes at the microscopic level, such as biochemical reaction rates.

S. Mitran (✉) and J. Young
Department of Mathematics, University of North Carolina, Chapel Hill,
NC 27599-3250, USA
e-mail: mitran@unc.edu

J. Young
e-mail: jendjoy@email.unc.edu

1 Introduction

The cytoskeleton is the scaffold animal cells use to interact mechanically with the environment. The cytoskeleton provides protection, enables movement, and determines cell shape. It is involved in most cellular processes and abnormalities in the cytoskeleton usually result in disease [34]. The role the cytoskeleton has in combating penetration of the cell by infectious micro-organisms, both mechanical and chemical, is presented in [37]. Hyperactive cytoskeleton reconfiguration has been associated with cancer (Fig. 1), and drugs targeting disruption of the cytoskeleton in cancerous cells are used therapeutically [34].

Qualitative understanding of the physiological role of the cytoskeleton has been rapidly accumulating. A quantitative link between overall mechanical properties of a cell and detailed biochemical reactions or microscopic configuration within the cytoskeleton is still lacking. Much progress has been made in characterizing small portions of the cytoskeleton or in constructing viable coarse grained models. Some of this work is reviewed below. Yet, the ultimate goal of linking therapeutic agents acting on the biochemistry of the cytoskeleton to mechanical properties of the entire cell is not fulfilled.

In this work we propose an approach to the fundamental computational modeling difficulty of describing a system that is not at equilibrium at microscopic scales. Full computational simulation at microscopic scales is prohibitively expensive. Coarse grained simulation at larger scales is incomplete, typically requiring the specification of a time-varying constitutive law that encapsulates missing microscopic information. Here we apply a general algorithm [29] for non-equilibrium multiscale phenomena. The basic approach detailed in Sects. 3–6 is to simultaneously advance forward in time continuum, kinetic, and molecular descriptions of the cytoskeleton. At the continuum level the cytoskeleton is treated as a plastic material with properties that vary in space and time. The kinetic level of description consists of evolution equations for probability distribution functions characterizing the microscopic system. Moments of the probability distribution functions provide constitutive closures needed at the continuum level. Microscopic ensembles constructed from the probability distribution functions are used to

Fig. 1 Carcinoma cell with multiple small blebs. (Image by Anne Weston, London Research Institute, Cancer Research UK, copyright Wellcome Images)
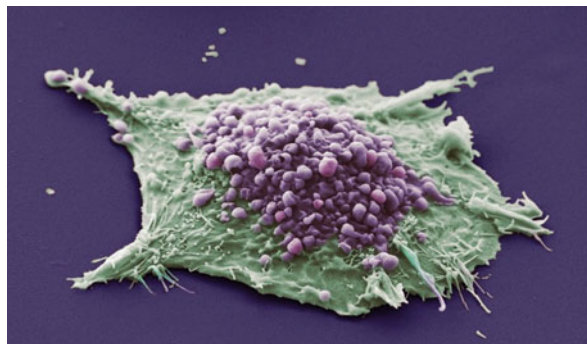
furnish initial conditions for simulations at a quasi-molecular level for small actin segments that makes up the cytoskeleton. The main difficulty in such multiscale computation is information transfer between scales. Minimal entropy changes of the kinetic probability distributions and optimal transport ideas are used in this work.

The presentation is organized as follows. An overview of cytoskeleton structure and current computational models is presented in Sect. 2. Section 3 presents an overview of the overall computational procedure and introduces notation. Section 4 presents the microscopic, kinetic, and continuum models of the cytoskeleton respectively. Some results on the overall model are shown in Sect. 5 and conclusions and further work are presented in Sect. 6.

2 The Cytoskeleton

A typical animal cell is approximately 10 μm in diameter, and consists of organelles (such as the nucleus, mitochondria) suspended in a fluid cytosol surrounded by the cytoskeleton. All of these cellular components are encased by a thin plasma membrane. The cytoskeleton of the animal cell is a complex structure that gives the cell mechanical support and integrity [1, 30]. This dynamic network of intertwined filaments participates in and orchestrates many cellular activities such as cell migration, mitosis, apoptosis and mechanotransduction [30].

2.1 Actin Filaments

The protein polymers that comprise the cytoskeleton include actin filaments, microtubules and intermediate filaments [1, 4, 30], and these fibers are crosslinked to one another by proteins such as filamin and α-actinin [1]. The main types of filaments participating in protrusive activities such as blebbing and lamellipodium formation are actin polymers. Actin filaments are long polymer chains built from actin protein subunits. These subunits are approximately 5 nm in diameter [1]. Free monomers of actin carry a molecule of ATP and are known as G-actin or globular-actin. When a G-actin subunit joins a growing polymer chain the ATP molecule is hydrolyzed into ADP and the subunit is attached. The actin protein in filament form is known as F-actin (filamentous-actin). Actin filaments have different rates of growth and shrinkage at their two ends. The "plus" end has a faster rate of elongation and shortening than the "minus" end [1]. The subunits in a filament are held together by weak, noncovalent bonds that can be broken by thermal fluctuations [1]. Actin subunit chains are often bound together in parallel to form a stronger double-stranded helical structure.

Filament length can vary depending on cell type, but they generally are 1–20 μm long and about 8 nm wide [4, 21]. They can be as long as 50–100 μm

in muscle cells [20], and as short as 0.2–0.35 μm in cytoskeleton meshes [8]. In either case, they are several orders of magnitude longer than they are wide.

Actin filaments are classified as semi-flexible polymers [21]. A single actin filament can withstand an elongation force of about 110–250 pN before breaking, and it only stretches about 0.2–0.3% under these forces [21]. It has a stiffness of approximately 45–65 pN/nm for actin filaments of length 1 μm [21]. On average, the Young's modulus of an actin polymer is 0.5 to 2×10^9 N/m^2 [4, 21]. In comparison to stretching, actin filaments bend quite easily. Their flexural rigidity has been found to be on the order of 10^{-26} N/m^2, based on a persistence length of 10–20 μm [4]. This large difference in magnitude between the stretching and bending properties of actin filaments allows them to be classified as an elastic string for modeling purposes.

The total number of actin filaments within a cell varies by cell type and concentration levels of actin. In red blood cells, actin fibers form a one to two filament thick network of short filaments [39]. This amounts to approximately 120,000–300,000 short actin filaments in a red blood cell cytoskeleton. Boal estimates that cells with high actin densities of 5 mg/ml or more, have approximately 1.9×10^{20} filaments length 1 μm^3 [4]. This translates to about 200,000, 1 μm filaments in a 10 μm diameter animal cell.

2.2 Filament Networks

The cytoskeleton is a mesh-like actin structure with crosslinks formed by proteins such as spectrin and filamin. Spectrin is a long 100 nm, flexible protein found close to the intracellular side of the plasma membrane. Two spectrin molecules link together head to head to create two actin filament binding sites that are spaced approximately 75–200 nm apart depending if the spectrin polymer is in a convoluted position or stretched out straight [1, 4]. This distance is quite large compared to the other proteins which bind actin bundles in tight configurations about 14–30 nm apart, and leads to large flexibility in the cytoskeleton. For example, the ability of red blood cells to deform enough to squeeze through capillaries is associated with the low spectrin spring constant of approximately 2×10^{-6} J/m^2. Filamin is another binding protein that crosslinks two filaments together almost at right-angles to one another forming a loose grid of actin polymers [1, 30]. Filamin is also found binding the actin mesh to the plasma membrane in platelets.

Binding of the actin network to the plasma membrane is also accomplished by other proteins. In muscle cells, the dystrophin protein carries out this role. In red blood cells, a protein in the plasma membrane known as band 3 attaches to another protein called ankyrin which in turn attaches to the spectrin proteins on the cytoskeleton [1]. Other adhesive proteins include ezrin, radixin, and moesin [1] (Fig. 2).
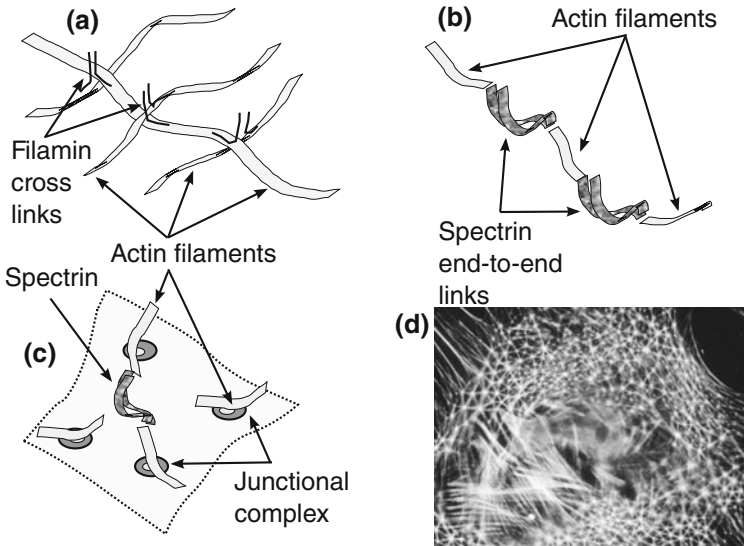
Fig. 2 Diagrams of actin network formation and attachment to plasma membrane. **a** Almost right-angle filamin crosslinks between actin filaments. **b** Spectrin end-to-end links. **c** Attachment to plasma membrane. **d** Micrograph of cytoskeleton in a fibroblast (Catherine Nobes and Alan Hall, copyright Wellcome Images)

The cytoskeleton is typically between 5 nm and 2-microns thick [11, 39]. The size of the gaps in the actin mesh range from 10 to 100 nm [12, 38, 40], depending on cell type. The aggregate elastic moduli of an actin network differ markedly from the single filament values. For instance, the estimated Young's modulus for 1 mg/ml of crosslinked F-actin is 100, 000 dyn/cm^2 which is 10 kPa and the shear modulus is approximated at 1, 000 dyn/cm^2 or 100 Pa [21]. Charras et al. [12] estimated the elastic modulus of the actin cortex in a filamin-depleted melanoma cell line to be 1–3 kPa. In general, the Young's modulus for the actin network is lower than the individual actin filaments. This is due to the fact that crosslinking proteins such as spectrin are more elastic than actin, so they make the overall mesh less stiff.

The cytoskeletal network is acted upon by myosin II motor proteins that produce forces between actin filaments [1, 24, 28, 33]. Such forces play a central role in the cell's protrusive and locomotive activities. Myosin II, like actin, is found in all eukaryotic cells [1]. Myosin II is a long protein composed of two heavy chains and two light chains. Near the end of the two heavy chains is a "head" region from which forces can be generated [1]. Myosin II subunits join to form a filament by bundling their tails together. This creates a bipolar filament with myosin heads facing in opposite directions along the fiber. Alternating myosin heads can attach to actin and exert a force ranging from 0.8 to 8 pN [4, 12, 41].
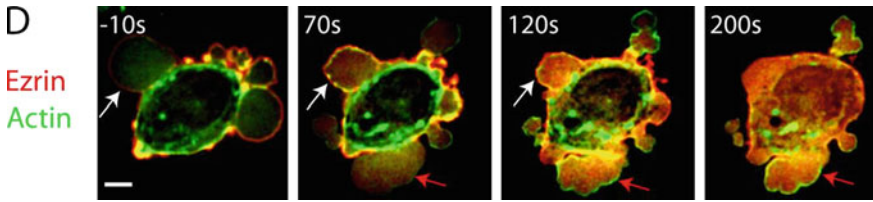
Fig. 3 An expanding and retracting bleb. Actin is labelled in *green*. After the bleb has fully inflated (frame 2), actin that arrives in the bleb builds a new cortex leading to bleb retraction [11]

2.3 Cellular Blebbing

Breakdown, rearrangement and rebuilding of the cytoskeleton produces various types of cellular protrusions which include lamellipodia, microvilli and blebs. A bleb is a balloon-like, cytosol-filled protrusion of the plasma membrane. Unlike lamellipodia and microvilli, this type of protrusion is not formed by active growth and rearrangement of the cytoskeleton [12, 14]. The onset of bleb formation is triggered by a contraction of the actin network, such that it detaches from the plasma membrane over some region. A gap size of 0.5–1 μm in the cytoskeleton/membrane connections is enough to initiate bleb formation [39]. Once a gap is formed, the typical 20–300 Pa [10, 35] overpressure in the cytosol with respect to ambient leads to bleb formation in 3–7 s. Typical bleb diameters range from 1 to 10 μm [11]. The bleb stays fully inflated for about 10–20 s. After this time interval, enough free actin monomers have begun to reorganize the cytoskeleton inside the bleb for retraction to occur [11]. The new cortex is built to a thickness of 10–20 nm (3–4 actin filaments thick) with gap sizes of approximately 200 nm [11] (see Fig. 3). Myosin II, present in this new cytoskeleton, creates contractions which pull the blebbed membrane inward to be reattached to the base cytoskeleton [11, 24].

2.4 Computational Challenges

The main difficulty in building realistic computational models of the cytoskeleton is the large number of filaments, the role of binding and motor proteins, and the dynamic nature of the network. Homogenized models of the cytoskeleton treated as a continuum are of limited utility since the elastic properties change in time as new links are formed and broken between actin filaments at a microscopic level. There are about 10^5 one-micron long filaments in a typical cell [4]. The filaments are crosslinked and the typical length of a filament segment between crosslinks is on the order of 100 nm [43]. This means there are approximately 10^6 filament segments in the cytoskeleton and roughly 5×10^5 crosslink protein complexes. The time scale of the cytoskeleton network is set by rate constants for actin polymerization, binding of various proteins to the network, myosin stepping rates,

and the elastic behavior of individual actin filaments. Time steps on the order of 10^{-6} s are required to capture all mentioned phenomena, leading to 3×10^7 time steps over the 30-s duration of a typical bleb. Evolving a system with approximately $N = 3 \times 10^6$ degrees of freedom over 3×10^7 time steps is prohibitively expensive since crosslink formation implies a computational complexity of the algorithm of $\mathcal{O}(N^2)$.

2.5 Current Work on Cytoskeleton

Given the aforementioned difficulties of direct numerical simulation at the scale of actin segments, much prior work has focused on constructing simplified models. A more complete review is available in the book by Kamm and Mofrad [23].

2.5.1 Coarse Grained Models

Coarse graining of the cytoskeleton degrees of freedom has been used by Li et al. [26] and Pivkin et al. [32] to create models of the red blood cell cytoskeleton during deformation. Simplification of the network geometry has been investigated by Boey et al. [5] using a sixfold, two-dimensional network. Palmer et al. [31] use the eight-chain symmetric network proposed by Arruda and Boyce [3] to deduce a constitutive model for the stress–strain relationship of actin networks which compares favorably with experimental work of Gardel et al. [15].

2.5.2 Detailed Microscopic Models

The coarse-grained models gloss over the details of the microscopic structure. To elucidate whether this is an acceptable hypothesis several research groups have undertaken the task of thoroughly modeling a small portion of the cytoskeleton to understand its mechanical response to various stresses. Kwon et al. [25] consider a 400^3 nm^3 block with approximately 100 crosslinked filaments of 350 nm length represented as elastic Euler–Bernoulli beams to determine the components of a general elastic tensor C_{ijkl} in the linear elasticity regime $\sigma_{ij} = C_{ijkl}\varepsilon_{kl}$ (σ, stress tensor; ε, strain tensor). The model performs well for isotropic and nearly isotropic systems, but exhibits large errors when the distribution of filament orientations is far from uniform. In a similar study, Huisman et al. [18] create an actin network model to examine its mechanical behavior under shear strain. The filaments were found to reorient themselves in the direction of applied shear, and the computed shear stiffening was compared to experimental findings. They conclude that the response of the network is highly dependent upon the topology of the filament mesh. Head et al. [16] explore the response of two-dimensional model networks to extensional and shear stresses to determine how strain is distributed in such

networks, dependent on crosslink density and filament length. They distinguish two distinct regimes, one where strains are uniformly distributed (affine deformation) and another in which strains are non-uniformly distributed (non-affine deformation). Buxton et al. [7] recently present a dynamic computational model in which an initial network comprising 100 one-micron long actin filaments undergoes polymerization and depolymerization. The filaments can also undergo capping, severing and crosslinking. The network develops until it reaches a statistical steady state and is then placed under shear stress in order to examine its mechanical response. Different networks were built based on different actin dynamics rates, and the mechanical responses of these networks were compared. The networks upon which these simulations were carried out typically consisted of approximately 10^2–10^3 filaments of lengths 2–9 μm, with about 10^3 crosslinks connecting them. Each simulation took about 100 h of CPU time.

2.5.3 Tensegrity Models

The tensegrity (tensional integrity) model of the cell was introduced in 1993 by Ingber in [19] to model the deformation of cells adhering to a substrate. This model consists of two types of prestressed elements: interconnected tension-bearing elements which represent the actin filaments of the cytoskeleton and compression-bearing elements, which represent microtubules [40]. This model assumes that the cell's shape and integrity derives from the cytoskeleton, an active mechanical structure capable of producing tension. The model is successful at capturing the strain-hardening observed in cells spreading over a substrate. However, it does not address the cytoskeleton's ability to rearrange and remodel itself during deformation. Stamenovic et al. [40] used this tensegrity model to analytically compute upper and lower bounds for the Young's modulus of cells. They compare their results against experimental data, finding that the empirical moduli in general fall within their theoretically derived bounds.

2.5.4 Continuum Models

The models discussed so far have been discrete in nature, characterizing the cytoskeleton as a network of crosslinked filaments. There is also a body of research dedicated to the treatment of the cytoskeleton as a continuum. Alt and Dembo [2] use a two-phase fluid description of the cytoplasm in ameboid cells. The cytosol (water-like substance within the cell) is represented as a Newtonian fluid, and the cytoskeleton is represented as a highly viscous, polymeric fluid. This characterization is used under the assumption that the crosslinks in the cytoskeleton are constantly rearranging, allowing the network to adapt and move easily (like a fluid). This model is used to simulate the formation of a lamellipodium during cell migration. During this phenomenon, the cytoskeleton undergoes many structural rearrangements. The model of Alt and Dembo is used for understanding

the general stages of this process. Charras et al. [9, 12], characterize the cytoskeleton as a solid porous medium. They propose that the actin network with interspersed cytoplasmic fluid should be thought of as a "sponge" with pressure diffusion occurring over time. They demonstrate experimentally that localized contractions of the actin mesh can create local pressure increases that do not instantaneously equilibrate across the cell. They develop a linear constitutive law for the cytoskeleton/cytosol complex using concepts from mixture theory. The stress–strain relationship is of the form: $\sigma = E\varepsilon - p$, with σ the stress, E the bulk elasticity modulus, ε the strain, and p the fluid pressure. Darcy's law for flow through porous media is used to update the fluid pressure term. Their theoretical model was developed to explain the cellular phenomenon of bleb formation.

2.6 Open Questions in Computational Cytoskeleton Models

The fundamental difficulty in all the above models is that experimental observations of cellular cytoskeletons highlight the dynamic nature of the network. While homeostatic behavior might reasonably be captured by coarse grained models, there is significant interest in large changes in cytoskeleton configuration since such changes are often associated with diseased states. Elucidating cytoskeleton behavior in such situations might suggest therapeutic approaches. The continuum models of Alt and Dembo [2] and Charras et al. [9, 12] represent the microstructure of the polymer network through a constitutive closure law. This constitutive law is complex and time-varying, and dependent on the microstructure of the medium. Without representing this microstructure in some way, the models in [2] and [9] do not reflect the changes and rearrangements occurring in the cytoskeleton that lead to varying mechanical properties. The detailed microscopic models that treat small portions of the cytoskeleton provide a great deal of insight into the mechanical response of small patches of actin networks, but do not apply to the entire cellular network due to the inhomogeneity and anisotropy of the cytoskeleton. Huisman et al. [18] specifically state that the stiffness response of the network is highly dependent on the concentrations of the different proteins in the cytoskeleton. These protein levels can certainly vary in different parts of the cortex as the cell undergoes locomotion and shape change. The detailed microscopic models also highlight the consequences of increasing anisotropy as the cytoskeleton is observed at smaller scales, especially the non-affine distribution of strain.

3 Overview of Computational Procedure

As seen from the previous section the main challenge in quantitative cytoskeleton modeling is efficient coupling of phenomena occurring at different length scales.

The cell is subject to forces that vary over a length scale comparable to the cell diameter $D = \mathcal{O}$ (10 μm). The response to these forces is a rearrangement of the actin filaments forming the cytoskeleton at the scale of average mesh spacing $l = \mathcal{O}$ (100 nm). The cytoskeleton rearrangement response is at time scales comparable to those arising from continuum level unsteady forces during protrusion and blebbing. There is no time scale separation and the microscopic configuration of the cytoskeleton is not at equilibrium.

In this work we apply a general multiscale interaction procedure, the time-parallel continuum–kinetic–molecular (tP-CKM) algorithm [29]. This algorithm is specially constructed to treat processes not at equilibrium at the microscale. A short overview of the algorithm is presented here, with further details available in [29]. The algorithm is constructed from three solvers for each length scale, and procedures for interscale communication. The three solvers are as follows.

1. *Continuum-level solver.* This may be any numerical approximation procedure for PDEs, e.g. discontinuous Galerkin, finite difference, finite volume. A finite volume procedure is exemplified here. The continuum variables are denoted by $\boldsymbol{Q}(\boldsymbol{x}, t)$. The evolution operator that advances the continuum variables from time t to time $t + \Delta t$ at position $\boldsymbol{x}$ is denoted by $\boldsymbol{C}$,

$$\boldsymbol{Q}(\boldsymbol{x}, t + \Delta t) = \boldsymbol{C}(t, t + \Delta t, \boldsymbol{Q}(\boldsymbol{x}, t), \psi(\boldsymbol{x}, t, \boldsymbol{q})). \tag{1}$$

The continuum operator depends on the microscopic configuration described by the probability distribution function (p.d.f.) $\psi \boldsymbol{x}, t, \boldsymbol{q})$ for the microscopic variables $\boldsymbol{q}$. Typically only a few integrals of $\psi(\boldsymbol{x}, t, \boldsymbol{q})$ are required,

$$\int g_i(\boldsymbol{q}) \psi(\boldsymbol{x}, t, \boldsymbol{q}) \mathrm{d}\boldsymbol{q} = G_i(\boldsymbol{x}, t), \quad i = 1, 2, \dots, M. \tag{2}$$

The specific form of $g_i(\boldsymbol{q})$ is problem-dependent.

2. *Kinetic-level solver.* The p.d.f. $\psi(\boldsymbol{x}, t, \boldsymbol{q})$ can be constructed from known microscopic transition probabilities between states $(\boldsymbol{q}', t')$ and $(\boldsymbol{q}, t)$,

$$P(\boldsymbol{q}, t | \boldsymbol{q}', t'). \tag{3}$$

Some specific physical model of the microscopic system furnishes $P(\boldsymbol{q}, t | \boldsymbol{q}', t')$. At some later time $t + \Delta t$ the p.d.f is given by

$$\psi(\boldsymbol{x}, t + \Delta t, \boldsymbol{q}) = \int P(\boldsymbol{q}, t + \Delta t | \boldsymbol{q}', t) \psi(\boldsymbol{x}, t, \boldsymbol{q}') \mathrm{d}\boldsymbol{q}'. \tag{4}$$

The transition probabilities can be characterized in various ways. One choice is to use the moments of the random variables $\boldsymbol{q} = (q_1, \dots, q_m)$. Assume, for simplicity of presentation, that the components of $\boldsymbol{q}$ are independent. Then the moments can be expressed as

$$\boldsymbol{\mu}_n(\boldsymbol{q}', t, \Delta t) = \int (\boldsymbol{q} - \boldsymbol{q}')^n P(\boldsymbol{q}, t + \Delta t | \boldsymbol{q}', t) \mathrm{d}\boldsymbol{q}, \tag{5}$$

and Taylor series expansion leads to

$$\boldsymbol{\mu}_n(\boldsymbol{q}, t, \Delta t)/n! = \boldsymbol{D}^{(n)}(\boldsymbol{q}, t)\Delta t + \mathcal{O}(\Delta t^2). \tag{6}$$

This Kramers–Moyal expansion leads to the evolution equation

$$\frac{\partial \psi(\boldsymbol{x}, t, \boldsymbol{q})}{\partial t} = \sum_{n=1}^{\infty} \left(-\frac{\partial}{\partial \boldsymbol{q}}\right)^n \boldsymbol{D}^{(n)}(\boldsymbol{q}, t)\psi(\boldsymbol{x}, t, \boldsymbol{q}). \tag{7}$$

The Fokker–Planck equation [36] arises from probability distribution functions completely characterized by the first two expansion coefficients $\boldsymbol{D}^{(1)}(\boldsymbol{q}, t), \boldsymbol{D}^{(2)}(\boldsymbol{q}, t)$.

3. *Molecular-level solver.* At the molecular level the system is assumed to be described by stochastic differential equations for the microscopic variables $\boldsymbol{q}(t)$. The time evolution operator is denoted by $\boldsymbol{M}$,

$$\boldsymbol{q}(t + \delta t) = \boldsymbol{M}(t, t + \delta t, \boldsymbol{q}(t)). \tag{8}$$

The relationship between continuum and microscopic variables will depend on the specific physical problem considered.

The tP-CKM algorithm advances the above solvers as depicted in Fig. 4. The overall goal is to advance the continuum variables over the time step $[t^k, t^{k+1}]$. The spatial dependence on $\boldsymbol{x}$ is suppressed for simplicity of presentation. Initial values for the continuum variables $\boldsymbol{Q}(t^k)$ and the p.d.f. $\psi(t^k, \boldsymbol{q})$ are assumed to be known from either a previous time step or physically specified initial conditions. The following steps are taken in the algorithm:

1. A continuum closure relation is computed from $\psi(t^k, \boldsymbol{q})$ using (2).
2. The continuum variables are advanced to time t^{k+1} using (1).
3. A new p.d.f. estimate at t^{k+1} is constructed, $\bar{\psi}^{(0)}(t^{k+1}, \boldsymbol{q})$, through a minimum entropy change with respect to $\psi(t^k, \boldsymbol{q})$ that reflects new continuum values. The

Fig. 4 Schematic of tP-CKM algorithm. *Boldface numbers* correspond to algorithm steps described in text. Portions of the algorithm executed serially in time depicted with *bold arrows*. Portions of the algorithm executed parallel in time depicted with *lighter arrows*
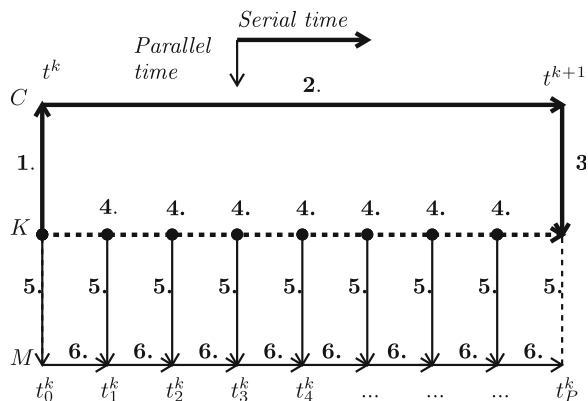
zero superscript indicates that this is a first approximation in an iterative refinement update.

4. The time interval $[t^k, t^{k+1}]$ is subdivided by intermediate time values $\{t^k = t_0^k, t_1^k, \ldots, t_P^k = t^{k+1}\}$. At each intermediate time value an estimate, $\bar{\psi}^{(0)}(t_j^k, \boldsymbol{q})$, of the p.d.f. is constructed using optimal transport theory.

5. From each approximate p.d.f. $\bar{\psi}^{(0)}(t_j^k, \boldsymbol{q})$ molecular-level ensembles $\mathcal{E}_j(t_j^k)$ are constructed.

6. The molecular-level ensembles are evolved forward in time to state $\mathcal{E}_j(t_{j+1}^k)$.

7. A density estimation procedure is applied to the updated molecular-level ensembles to obtain a new estimate of the p.d.f. based upon molecular level information, $\tilde{\psi}^{(0)}(t_{j+1}^k, \boldsymbol{q})$.

8. The p.d.f. estimates from minimal entropy modification and optimal transport are compared to those from the molecular level computation at the end of the continuum time step by computing an error

$$\varepsilon^{k+1} = \|\bar{\psi}^{(0)}(t^{k+1}, \boldsymbol{q}) - \tilde{\psi}^{(0)}(t^{k+1}, \boldsymbol{q})\|. \tag{9}$$

If within some tolerance, the continuum time step is accepted, and the new p.d.f. is also available for the next time advancement to t^{k+2}. If the error is too large, steps 3–7 are repeated.

The kinetic-molecular part of the algorithm can be seen as a multiphysics generalization of the parareal algorithm [27] for time-parallel solution of systems of ordinary differential equations. Whereas the parareal algorithm uses two different numerical discretizations of the same ODE system, the tP-CKM algorithm uses two different mathematical models of the same underlying physical system. One description is through p.d.f.'s describing the microscopic variables, and another description is through direct numerical simulation at the microscopic level.

Though apparently costly, the tP-CKM algorithm can be made computationally efficient by:

1. time-parallel execution at the kinetic level using P processors that work independently over each subinterval $[t_j^k, t_{j+1}^k]$;

2. further massive parallelization of the stochastic differential equations (SDEs) at the molecular level through use of modern graphics processing units (GPUs).

The iterative refinement comprising steps 3–7 of the algorithm builds ever more accurate estimates of the p.d.f.'s at times $\{t_1^k, \ldots, t_P^k\}$. The hope is that much fewer than P refinement stages will lead to an acceptable precision in (9). Indeed if P refinement stages are needed, then the physical system would have been evolved at the microscopic level over the entire continuum time step $[t^k, t^{k+1}]$ and nothing would have been gained by the multiscale interaction procedure. Numerical experiments reported below show that very few iterative refinement stages (e.g. 1–3) are needed to obtain 3–4 significant digits of precision in continuum-level variables. The time-parallelization allows large numbers of processors to be used, e.g. $P \simeq 1,000$ leading to significant reductions in wall-clock execution time.

One of the key aspects of such a continuum–kinetic–molecular (CKM) algorithm is the set of procedures for communicating data between different levels of description. For the continuum-to-kinetic step these procedures are:

1. A minimum entropy modification of the kinetic-level p.d.f. at time t^{k+1} to reflect information available from the continuum level;
2. Modification of the p.d.f. at times $\{t_1^k, \ldots, t_{P-1}^k\}$. by use of optimal transport theory.

A brief description of each procedure is provided here with fuller details available in [29].

3.1 Minimal Relative Entropy Modification

Consider the Kullback–Leibler [13] relative entropy functional

$$H(\psi^{k+1}, \psi^k) = \int \psi^{k+1} \log\left(\frac{\psi^{k+1}}{\psi^k}\right) d\boldsymbol{q}, \qquad (10)$$

which expresses the "information distance" of ψ^{k+1} with respect to ψ^k (note that it is not a distance function in the mathematical sense). After taking a continuum time step, new constraints are imposed on ψ^{k+1}. By this means boundary conditions at the continuum-scale are efficiently transferred to kinetic and hence microscopic scales. The general form of a constraint is

$$\int f_i(\boldsymbol{q})\psi^{k+1}(\boldsymbol{q})d\boldsymbol{q} = F_i(\boldsymbol{Q}^{k+1}), \quad i = 1, 2, \ldots, L. \qquad (11)$$

We seek to determine the p.d.f. that has the minimum information change with respect to the previous time step but reflects the new constraints. Instead of solving the constrained optimization problem, Lagrange multipliers $\lambda_i, 1 \leqslant i \leqslant L$ are introduced and the unconstrained problem

$$\inf_{\lambda_i} \sup_{\psi} \left[-H(\psi|\psi^k) + \sum_{i=1}^{L} \lambda_i \left(\int f_i(\boldsymbol{q})\psi^{k+1}(\boldsymbol{q})d\boldsymbol{q} - F_i(\boldsymbol{Q}^{k+1}) \right) \right], \qquad (12)$$

is solved.

3.2 Optimal Transport of Probability Density

The minimal entropy modification problem (12) is rather expensive to solve computationally because of the large-dimensional phase–space integrals of the form $\int d\boldsymbol{q}$, especially in the context of rapidly providing estimates of a p.d.f. at the

intermediate times $\{t_1^k, t_2^k, \ldots, t_{P-1}^k\}$. in order to carry out time parallel computations. An immediate idea would be to carry out linear interpolation between ψ^k and $\bar{\psi}^{k+1}$. In the context of solving Fokker–Planck equations at the kinetic level, this would basically correspond to linear response theory [36].

It is however of interest to construct better intermediate estimates given the endpoint p.d.f.'s $\psi^k, \bar{\psi}^{k+1}$, especially estimates that capture the microscopic physics of the system. Optimal transport theory [42] can be used to this end.

Given $\mu : A \to \mathbb{R}$, $v : B \to \mathbb{R}$, two p.d.f.'s, the optimal transport problem is to find a transference plan $T : A \to B$, such that for any subset $P \subset A$, whose image under the transference plan is $T(P) \subset B$, we have

$$\int_{x \in P} \mu(x)\mathrm{d}x = \int_{y \in T(P)} v(y)\mathrm{d}y. \tag{13}$$

Assuming T is a differentiable mapping, $T \in C^1(\mathbb{R}^d)$, the integral condition (13) implies the differential equation

$$\det(\nabla T(x))v(x) = \mu(x), \tag{14}$$

which is nothing more than the usual change-of-variable theorem in integral calculus.

Since there exist infinitely many differentiable mappings for which (14) holds, an optimization problem can be posed, in which a specific mapping is sought that has some desirable properties. One possibility is to introduce a distance between the two p.d.f.'s μ, v as exemplified by the Wasserstein distance

$$d_p(\mu, v) = \left(\inf_T \int |T(x) - x|^p \mu(x)\mathrm{d}x \right)^{1/p}, \tag{15}$$

$d_p : A \times B \to \mathbb{R}$. The optimization (15) then seeks the transference plan closest to the identity mapping.

A number of remarkable results have shown the connection between optimal transport and several physical processes such as various types of fluid flow [6]. Here we focus on a result by Jordan, Kinderlehrer and Otto (JKO) [22] establishing a link between optimal transport and solutions of a Fokker–Planck equation. Consider a Fokker–Planck equation of the form

$$\frac{\partial \psi}{\partial t} = \frac{\partial}{\partial \boldsymbol{q}} \cdot \left(\frac{\partial \Phi}{\partial \boldsymbol{q}} \psi \right) + \frac{1}{\beta} \frac{\partial}{\partial \boldsymbol{q}} \cdot \frac{\partial \psi}{\partial \boldsymbol{q}}, \tag{16}$$

with $\Phi(\boldsymbol{q})$ a potential function in phase space. Associated with the p.d.f. $\psi(\boldsymbol{q})$ the free energy $F(\psi)$, internal energy $E(\psi)$ and entropy functionals $S(\psi)$ can be defined,

$$F(\psi) = E(\psi) + \frac{1}{\beta}S(\psi), \tag{17}$$

$$E(\psi) = \int \Phi(q)\psi(q)dq, S(\psi) = \int \psi(q)\log\psi(q)dq. \tag{18}$$

Let ψ_j^k be p.d.f.'s defined at the intermediate times t_j^k in the time interval $[t^k, t^{k+1}]$ with the constant spacing Δt. The JKO result [22] states that if the intermediate time $\psi_j^k(q)$ is chosen as the solution of the minimization problem

$$\min_{\psi}[\mathcal{F}(\psi)] = \min_{\psi}\left[\frac{1}{2}d_2\left(\psi^{(n-1)}, \psi\right) + (\Delta t)F(\psi)\right], \tag{19}$$

then in the limit $\Delta t \to 0$ we have

$$\psi\left(t_j^k, q\right) = \psi_j^k, \tag{20}$$

meaning that the solution of the minimization problems (19) is also the solution of the Fokker–Planck equation (16). Furthermore, at each point in time in the $[t^k, t^{k+1}]$ interval, the evolution of the solution to the Fokker–Planck equation follows the steepest descent direction of the function in (19).

This result is applied in the tP-CKM algorithm to construct nonlinear interpolations of p.d.f.'s at intermediate time steps. Consider a representation of the time-varying p.d.f. as

$$\psi(q, t) = \sum_{l=1}^{N_B} c_l(t)B_l(q), \tag{21}$$

with $B_l(q)$ some set of basis functions in phase space. Simple linear interpolation between times would lead to intermediate expansion coefficient values

$$c_l\left(t_j^k\right) = \frac{t_j^k - t^k}{t^{k+1} - t^k}\left[c_l(t^{k+1}) - c_l(t^k)\right] + c_l(t^k). \tag{22}$$

We can however exploit the steepest descent property from the JKO theorem to specify that the tangent direction of the interpolation of $\psi(q, t)$ in the space of coefficients c_l is given by the direction

$$\nabla_c \mathcal{F}(\psi). \tag{23}$$

With this information, a cubic interpolant can readily be constructed. A schematic of the difference between linear interpolation and the interpolation based on free-energy minimization is shown in Fig. 5. The principal benefit of this higher-order interpolation procedure is the reduction of iterative refinements between the kinetic and molecular stages.

4 A tP-CKM Model of the Cytoskeleton

We apply the computational framework described above to the problem of cytoskeleton mechanics. There is considerable scope for choosing a model at each

Fig. 5 Comparison between linear interpolation of p.d.f.'s in c-space and cubic interpolation based upon minimization of free energy
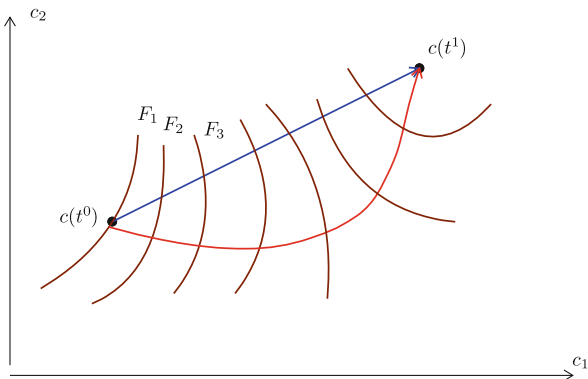
length scale, and the choices described are just one option, mainly made to obtain as simple a description as possible for this initial application of the tP-CKM algorithm to cytoskeleton mechanics. In particular we restrict attention to two-dimensional microscopic and one-dimensional continuum models at present.

4.1 Geometric Description of Cell Membrane, Cytoskeleton

The cell membrane is represented as a piecewise linear closed curve defined by points (X_i, Y_i), $i = 0, \ldots, N_m$. A curvilinear coordinate s is defined along the cell membrane. The cytoskeleton is assumed to be situated in a shell inside the cellular membrane and to have an average thickness $d(s)$. At the junction an outward pointing normal to the cell membrane $\mathbf{n}$ is defined along the bisector of the intersecting line segments. Displacement towards the interior of the cell by distance $d(s)/2$ defines a cytoskeleton centerline. The choice of a piecewise linear representation is motivated by the desire to capture deformations of arbitrary complexity (Fig. 6).

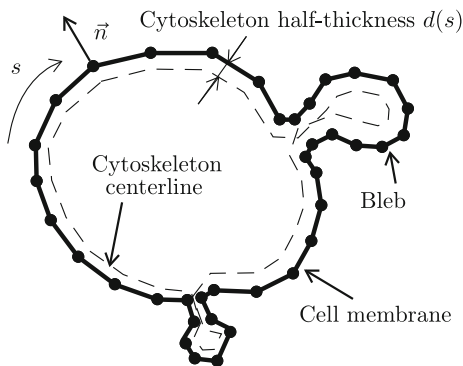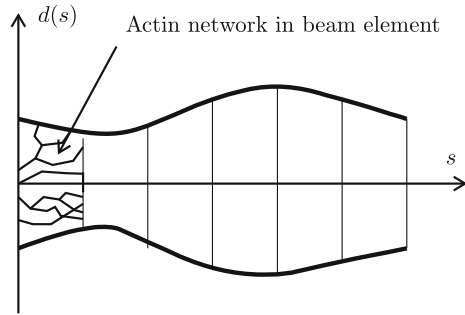**Fig. 6** Sketch of cellular membrane, cytoskeleton centerline

Fig. 7 Sketch of variable thickness beam composed of cross-linked filament elements model of cytoskeleton

The piecewise linear representation for the cellular membrane defines elements B_i from point (X_{i-1}, Y_{i-1}) to (X_i, Y_i), $i = 1, \ldots, N_m$. Each element has an average thickness d_i. At the continuum scale elements B_i are one-dimensional elastic bodies akin to nonlinear beams. At the microscopic scale each element B_i is formed from numerous actin filaments cross-linked in a network (Fig. 7).

4.2 Microscopic Description

A model for the formation and evolution of the actin network must be specified. This is done separately for each element B_i of the cytoskeleton that extends from s_{i-1} to s_i. Starting from s_{i-1}, N_f random walks with step-length a are generated by the following procedure.

1. Draw a direction θ from a probability distribution function ψ_θ.
2. Advance the random walk by a along direction $(\cos\theta, \sin\theta)$. Associate actin filament stretch stiffness μ with this step, and initial strain ε with this step as drawn from a probability distribution function ψ_ε.
3. With probability P_f start two new branches at angle $\varphi \simeq \pi/2$ to the current branch. This to models the nearly orthogonal cross-link formed by filamin.
4. With probability P_s generate a step of length b along the current direction θ. Associate spectrin stretch stiffness v with this step.
5. If the random walk step crosses the cell membrane attach the end point of the random walk step to the membrane with probability P_m.
6. Stop the random walk if the edge of the beam element at s_i is reached, or if the edge of the cytoskeleton at interior thickness d_i is reached.

The above simple model involves two p.d.f.'s, one for orientation (ψ_θ) and one to characterize the strain of each filament segment (ψ_ε). The orientation and strain of the filaments is expected to respond to imposed forces at the continuum scale. The probabilities P_f, P_s, P_m encapsulate the complicated biochemical reactions that form linkages between actin filaments. In this work we are basically interested in proof-of-concept computations and P_f, P_s, P_m shall be imposed rather than obtained from detailed chemical kinetics.

At the end of the above procedure we have N_i actin and spectrin segments defining the network inside of each beam element B_i. Let $\mathbf{r}_j$ be the position vectors of the endpoints of the segments, $j = 1, \ldots, M_i$. Some of these endpoints correspond to points on the membrane or on the beam element boundaries at s_{i-1} and s_i. The motion of these points is imposed as a displacement boundary condition at each moment in time. The other endpoints change position in response to elastic forces $\mathbf{F}_j(t)$ in the filament segments ending at that particular node and at time t. Inertial effects are negligible, and the equation of motion of these nodes is given by the Langevin equation

$$\eta\frac{d\mathbf{r}_j}{dt} = \mathbf{F}_j(\mathbf{r}, t) + \mathbf{w}_j(t), \tag{24}$$

with $\mathbf{w}_j(t)$ a Gaussian noise term of intensity given by the fluctuation-dissipation theorem, and $\mathbf{r} = (\mathbf{r}_1, \ldots, \mathbf{r}_{M_i})$. In order to more readily link the microscopic dynamics to the ψ_θ, ψ_ε p.d.f.'s it is convenient to consider the equation for the time evolution of the end-to-end vector of each filament,

$$\boldsymbol{\delta}_{jk} = \mathbf{r}_k(t) - \mathbf{r}_j(t), \tag{25}$$

that satisfies the SDE

$$\eta\frac{d\boldsymbol{\delta}_{jk}}{dt} = \mathbf{F}_k(\boldsymbol{\delta}, t) - \mathbf{F}_j(\boldsymbol{\delta}, t) + \mathbf{w}_k(t) - \mathbf{w}_j(t). \tag{26}$$

The orientation and strain of the filament are immediately available as

$$\theta_{jk} = \text{atan}\big[(\boldsymbol{\delta}_{jk} \cdot \mathbf{e}_y)/(\boldsymbol{\delta}_{jk} \cdot \mathbf{e}_x)\big], \varepsilon_{jk} = |\boldsymbol{\delta}_{jk}|/l_0 - 1, \tag{27}$$

with l_0 the undeformed length of the filament. Let (u_{jk}, v_{jk}) be the x, y components of the displacement $\boldsymbol{\delta}_{jk}$, such that $\theta_{jk} = \text{atan}(v_{jk}/u_{jk})$

Though simple, this microscopic model is capable of capturing strain-hardening through the ψ_θ p.d.f. and also retains memory of the previous strain state through ψ_ε.

4.3 Kinetic Description

The Fokker–Planck equation associated with the Langevin dynamics specified by (26) is

$$\frac{\partial\psi}{\partial t} + \frac{\partial}{\partial u}(F_u\psi) + \frac{\partial}{\partial v}(F_v\psi) = \frac{1}{\beta}\left(\frac{\partial^2\psi}{\partial u^2} + \frac{\partial^2\psi}{\partial v^2}\right), \tag{28}$$

with ψ a function of time and the filament end-to-end displacements, $\psi(t, u, v)$. The principal modeling difficulty is establishing the relationship between the

forces $\mathbf{F}_j(\boldsymbol{\delta}, t)$ defined in the microscopic description and some general functions $(F_u(u, v), F_v(u, v))$ needed in the kinetic-level equation (28).

The simplest approach is to assume that the elastic filament forces come from a potential

$$\boldsymbol{\Phi}(u, v) = \frac{\mu}{2}\Big[(u - U_i)^2 + (v - V_i)^2\Big], \qquad (29)$$

with (U_i, V_i) the average displacement in block B_i, a hypothesis that corresponds to affine distribution of strain among the filaments. It has been established by a number of researchers [17], that affine strain distributions are obtained at large densities of actin filaments, but that as the number of filaments decreases the strain distribution can differ markedly from the average strain in a control volume. The drawback of using an affine distribution of strain at the kinetic level is attenuated in the context of the tP-CKM algorithm. The probability distribution function $\psi(t, u, v)$ is used only to instantiate microscopic ensembles according to the procedure outlined in 4.1. The subsequent time evolution is however carried out at the molecular level by evolving the SDEs (26) forward in time, through what is assumed to be a physically correct model. The kinetic-level computation simply acts as a predictor step to be corrected by the molecular level evolution. The availability of a predictor step is computationally convenient since it furnishes the required approximation of the initial conditions at the time substeps $\{t_1^k, \ldots, t_{P-1}^k\}$, and thereby allows time-parallel computations. Also, the branching defined by step (3) of random walk procedure randomizes initial orientations with respect to the average strain direction specified by the potential (29).

An alternative to the affine deformation hypothesis expressed by (29) is to use a Kramers–Moyal expansion. During the microscopic evolution the first two moments of the probability transition function P $(u, v, t + \Delta t | u', v', t)$ can be computed by accumulating statistics from the numerical solution of the SDEs (26). The moments defined by

$$M_{m,n}(u', v', \Delta t) = \int (u - u')^m (v - v')^n P(u, v, t + \Delta t | u', v', t) \mathrm{d}u' \mathrm{d}v', \qquad (30)$$

are approximated by time sampling over n_t time steps, and an interpolation of the sampling can be used to determine the coefficients $\boldsymbol{D}^{(1)}(u, v, t) \in \mathbb{R}^2$, $\boldsymbol{D}^{(1)} = (D_u^{(1)}, D_v^{(2)}), \boldsymbol{D}^{(2)}(u, v, t) \in \mathbb{R}^{2 \times 2}$ needed in the Fokker–Planck equation

$$\frac{\partial \psi}{\partial t} + \frac{\partial}{\partial u}\Big(D_u^{(1)}\psi\Big) + \frac{\partial}{\partial v}\Big(D_u^{(1)}\psi\Big) = \frac{1}{\beta}\nabla_{(u,v)} \cdot \Big(\boldsymbol{D}^{(2)}(u, v, t)\nabla_{(u,v)}\psi\Big). \qquad (31)$$

Though capable of capturing non-affine strain distributions in the filament network, this approach is much more costly, due to the necessity of accumulating statistics. Tests in this work are done using affine instantiation of the filament network.

4.4 Continuum Description

In this simple model, the cytoskeleton is seen as a variable thickness, curved beam at the continuum level (Fig. 8).

Let $\mathbf{r}(s, t)$ be the position vector of a point along the one-dimensional beam model of the cytoskeleton, $\boldsymbol{\tau}(s,t)$, $\boldsymbol{v}(s,t)$ the tangent and normal vectors, and $\kappa(s, t)$ the curvature. Assuming slow, non-inertial motion the beam equation of motion in this case is

$$\eta\frac{\mathrm{d}\mathbf{r}}{\mathrm{d}t} = \Delta p(s,t)\boldsymbol{v} + \frac{\mathrm{d}}{\mathrm{d}s}\left(T\boldsymbol{\tau} + EI\frac{\mathrm{d}\kappa}{\mathrm{d}s}\boldsymbol{v}\right), \tag{32}$$

with Δp the difference between cytosol and ambient pressure, $T(s, t)$ the tension in the beam, and EI the flexural rigidity. For small displacements during a time step the flexural rigidity can be expressed as $EI = MR = M/\kappa$, with R the radius of curvature. The beam tension T is expressed in terms of the filament forces $\mathbf{f}$ as

$$T = \frac{1}{L_i}\left(\int_{B_i} \mathbf{f}\mathrm{d}s\right)\boldsymbol{\tau}, \tag{33}$$

with L_i the length of beam element B_i. The tension can also be expressed as an average over deformation states of the beam as

$$T = \mu \int (u\tau_x + v\tau_y)\psi(u,v)\mathrm{d}u\mathrm{d}v, \tag{34}$$

using the p.d.f. of displacement state $\psi(u, v)$, μ the stretching stiffness of a filament and (τ_x, τ_y) the components of the tangent vector. The moment in the beam can also be computed either as a spatial average

$$M = \frac{1}{L_i}\int_{-L_i/2}^{L_i/2} (\mathbf{f}\cdot\boldsymbol{v})s\mathrm{d}s, \tag{35}$$

Fig. 8 Sketch of pressure and cytoskeleton forces acting on cellular membrane elements
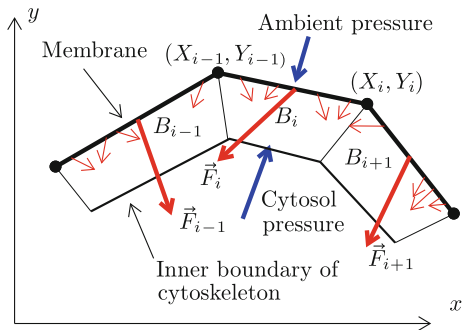
or an average over deformation states by evaluating

$$M = a\mu \int (uv_x + vv_y)\cos\theta\psi(u,v)\mathrm{d}u\mathrm{d}v\mathrm{d}\theta. \tag{36}$$

Expression (36) evaluates the torque of the filament forces normal to the beam element, over all possible filament displacements and orientations. Relations (33–36) furnish the requisite lengths between continuum and microscopic models. When seeking continuum closure relations from a known microscopic state the integrals (33–36) are evaluated directly.

Consider some numerical method applied to (32) to advance $\mathbf{r}(s, t^k)$ to a new time level t^{k+1}. The average displacements in beam element B_i of length Δs_i can be evaluated as

$$U_i^{k+1}\mathbf{e}_x + V_i^{k+1}\mathbf{e}_y = \left(\frac{\partial\mathbf{r}}{\partial s}\right)_i^{k+1}\Delta s_i. \tag{37}$$

These average displacements are imposed as constraints on the p.d.f. for the microscopic displacements at the new time level

$$U_i^{k+1} = \int u\psi(u,v,t^{k+1})\mathrm{d}u\mathrm{d}v, \quad V_i^{k+1} = \int v\psi(u,v,t^{k+1})\mathrm{d}u\mathrm{d}v, \tag{38}$$

constraints to be satisfied by the minimal entropy modification of $\psi(u,v,t^k)$.

5 Results

We now turn to a proof-of-concept computation. The parameters chosen here are meant to qualitatively capture blebbing phenomena, but no claim is made that this initial demonstration of the method accurately captures biological phenomena.

An initial circular shape is assumed for a cell of diameter $D = 10$ μm. The overpressure of the cytosol with respect to ambient is set as $\Delta p = 100$ Pa. The boundary is discretized in $N_m = 4 \times 10^3$ elements. Initial uniform distributions for the filament orientation are chosen in each element. In each element the random walk generation procedure is repeated until there are $N_i > 10^3$ actin filaments in each element, and at least $N_{c,i} > 50$ connections of the filaments in each element with the cellular membrane. Probabilities $P_m = 0.5$, $P_s = 0$, $P_f = 0.25$ are chosen in the network generation procedure. This corresponds to a 50% chance that a filament that crosses the cellular membrane attaches to the membrane, no spectrin elements, and that, on average, at every fourth random walk step of length $a = 20$ nm we encounter a crosslink. The system is allowed to equilibrate by advancing the SDEs (26) and constraining the motion of all nodes on the membrane to be along radii until the cytosol overpressure is balanced by stretching forces within the network. The sequence of shapes obtained during this equilibration
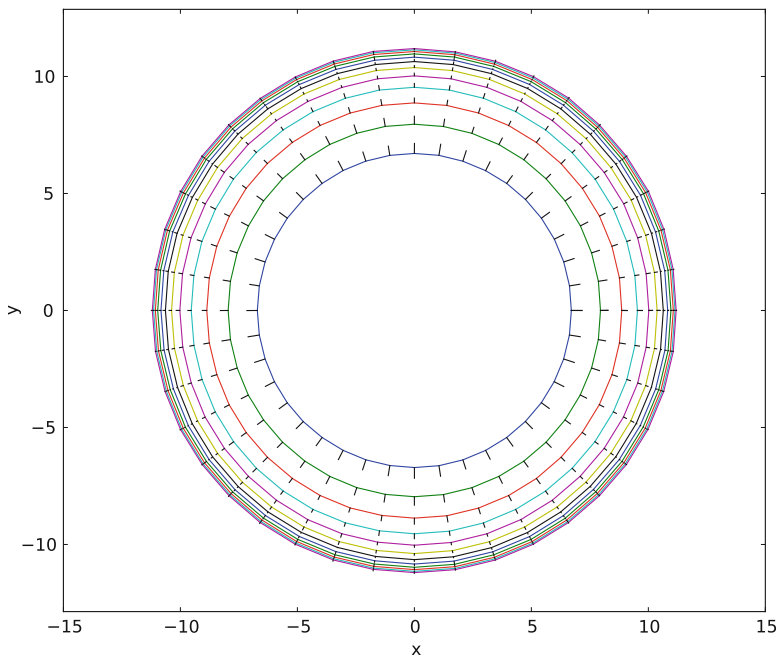
Fig. 9 Initial equilibration of a circular model of a cell. The forces on the membrane elements are shown by the line segments pointing outward from the circular cell model. Time slices at 10-s intervals from $t = 0$ to $t = 120$ s

process are shown in Fig. 9. The equilibration process is a non-trivial test showing that uniform distributions of the orientations of the filaments in each continuum block, and using sufficient filaments to have affine distributions of strain, maintains symmetry of the computation.

After the initial equilibration, the formation of blebs is simulated by modifying the probability of attachment of a filament to the membrane,

$$P_m(t) = 0.01 + 0.49 \left(1 - \frac{1}{1 + e^{20-t}} + \frac{1}{1 + e^{40-t}} \right), \qquad (39)$$

which models the formation of a bleb over an interval of 20 s, by changing the baseline membrane attachment probability from 0.5 to 0.01 (Fig. 10). The change is imposed on various regions of the cell, both localized to represent a small bleb and over large regions.

The main intent of these initial tests is to ascertain whether bleb formation occurs and is then retracted. Detachment of the cytoskeleton occurs as expected. A sequence of membrane shapes during the bleb formation stage is shown in Fig. 11. A detail of the formation of a small bleb is shown in Fig. 12. After some time ($t > 40$) the probability of reattachment of the cytoskeleton network to the membrane is set to the initial value $P_m = 0.5$ and the membrane reverts to a quasi-circular shape. Figure 13, shows the final stage of retraction of a small bleb.

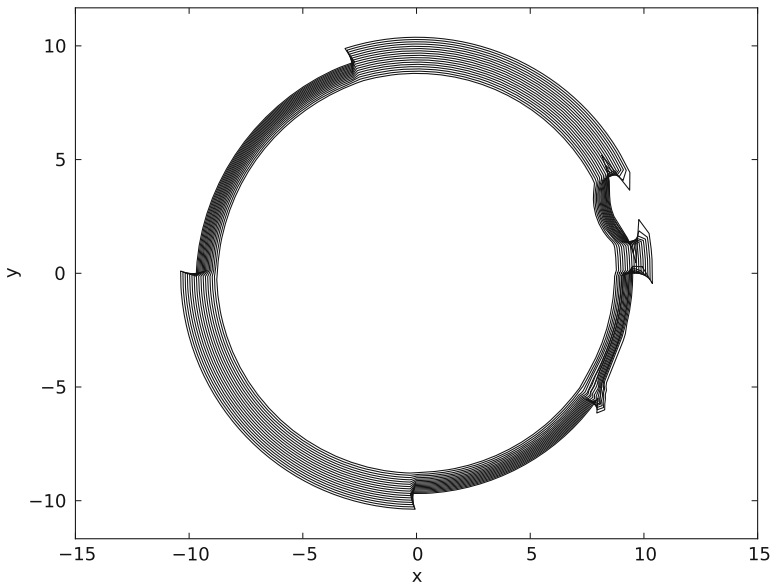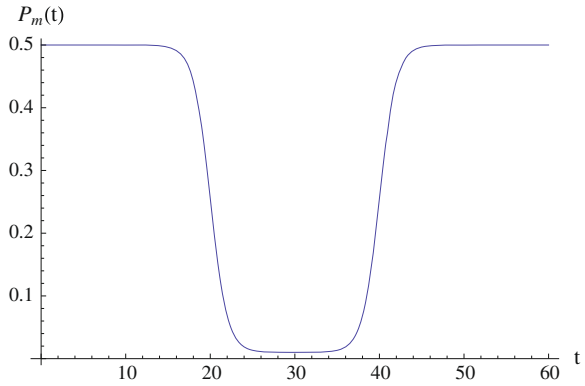**Fig. 10** Imposed time variation of actin filament to membrane attachment probability

Fig. 11 Sequence of membrane shapes at $\Delta t = 0.5$ s intervals from $t = 19$ to $t = 24$ s

6 Conclusions

Development of quantitative models that link overall cytoskeleton mechanical behavior to microscopic phenomena exemplified by biochemical reactions is a challenging endeavour. Such quantitative models are however of great interest since many diseased states manifest themselves at large scales, but are caused by breakdowns in biochemical processes at the molecular scale. In this work we have carried out an initial application of a general multiscale interaction framework
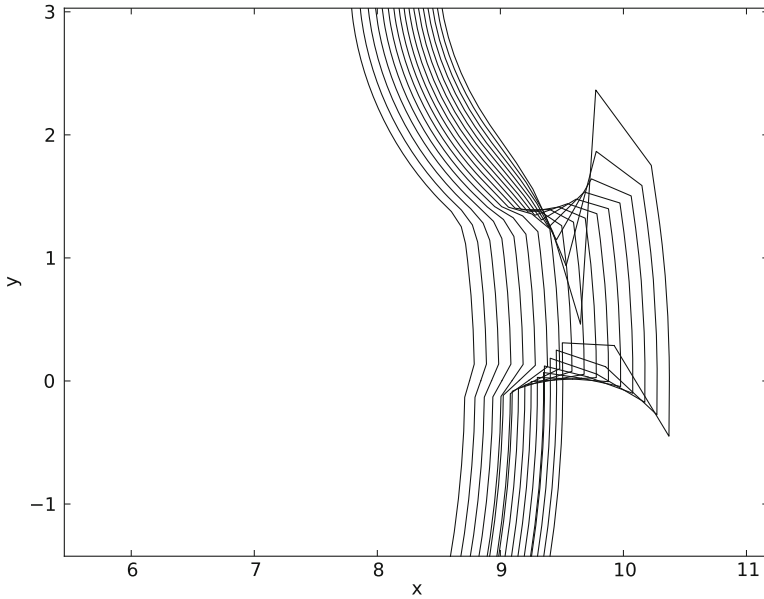
Fig. 12 Sequence of membrane shapes in bleb formation. ($\Delta t = 0.5$ s time intervals between successive membrane positions)
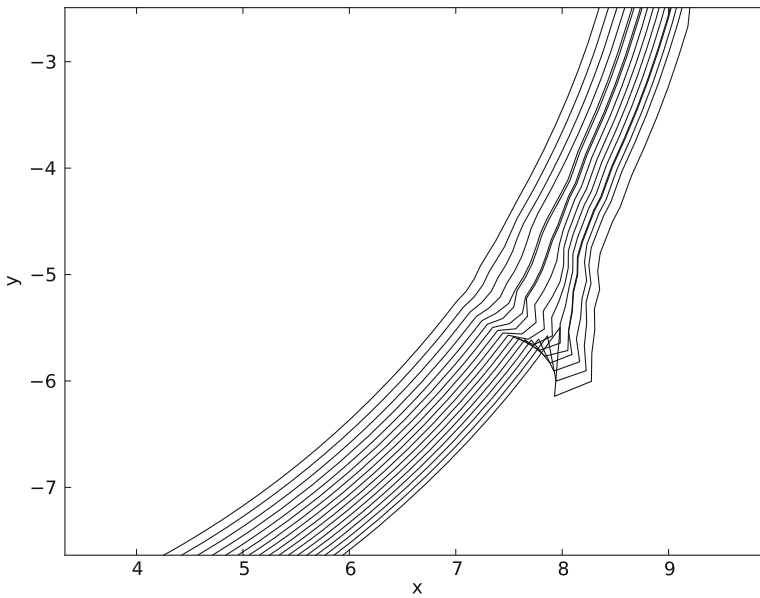

Fig. 13 Late stage retraction of a bleb ($\Delta t = 0.5$ s, from $t = 38$ to $t = 46$ s)

constructed to facilitate linkage between molecular and continuum phenomena. The main features of the tP-CKM framework that are of utility in constructing cytoskeleton models are:

1. The repeated regeneration of the cytoskeleton network through refined estimates of the p.d.f. ψ describing the network geometry mimics the continual rearrangement exhibited by real biological systems.
2. Time parallelization allows large-scale models to be simulated.
3. The interpolation between time steps of the p.d.f. using optimal transport theory allows larger continuum time steps to be taken by comparison to linear response Fokker–Planck theory.

This initial application of the tP-CKM framework to a simplified cytoskeleton model is not yet fully realistic. Biochemical kinetics must be included in the model in order to determine rates at which actin filaments form crosslinks or attach to the membrane in response to local concentrations. A model for the action of myosin on the network must be included. We have however shown that imposing smaller probabilities of filament to cellular membrane attachment does lead to the formation of a protrusion (a bleb) that is subsequently retracted when the actin network reforms. Work is underway to construct models that incorporate more of the known biology of the cytoskeleton.

References

1. Alberts, B., Johnson, A., Lewis, J., Raff, M., Roberts, K., Walter, P.: Molecular Biology of the Cell, 4th edn. Garland, New York (1994)
2. Alt, W., Dembo, M.: Cytoplasm dynamics and cell motion: two-phase fluid models. Math. Biosci. **156**(1–2), 207–228 (1999)
3. Arruda, E., Boyce, M.: A three-dimensional constitutive model for the large stretch behavior of rubber elastic materials. J. Mech. Phys. Solids **41**(2), 389–412 (1993)
4. Boal, D.: Mechanics of the Cell. Cambridge University Press, Cambridge (2002)
5. Boey, S., Boal, D., Discher, D.: Simulations of the erythrocyte cytoskeleton at large deformation I. Microscopic models. Biophys. J. **75**(3), 1573–1583 (1998)
6. Brenier, Y.: Optimal transport, convection, magnetic relaxation and generalized Boussinesq equations. J. Nonlinear Sci. **19**, 547–570 (2008)
7. Buxton, G., Clarke, N., Hussey, P.: Actin dynamics and the elasticity of cytoskeletal networks. Exp. Polym. Lett. **3**(9), 579–587 (2009)
8. Cano, M.L., Lauffenburger, D.A., Zigmond, S.H.: Kinetic analysis of f-actin depolymerization in polymorphonuclear leukocyte lysates indicates that chemoattractant stimulation increases actin filament number without altering the filament length distribution. J. Cell Biol. **115**, 677–687 (1991)
9. Charras, G.T.: A short history of blebbing. J. Microsc. **231**(3), 466–478 (2008)
10. Charras, G.T., Coughlin, M., Mitchison, T.J., Mahadevan, L.: Life and times of a cellular bleb. Biophys. J. **94**(5), 1836–1853 (2008)

11. Charras, G.T., Hu, C., Coughlin, M., Mitchison, T.J.: Reassembly of contractile actin cortex in cell blebs. J. Cell Biol. **175**(3), 477–490 (2006)
12. Charras, G.T., Yarrow, J.C., Horton, M.A., Mahadevan, L., Mitchison, T.J.: Non-equilibration of hydrostatic pressure in blebbing cells. Nature **435**, 365–369 (2005)
13. Cover, T.: Elements of Information Theory. Wiley, New York (1991)
14. Cunningham, C.C.: Actin polymerization and intracellular solvent flow in cell surface blebbing. J. Cell Biol. **129**(6), 1589–1599 (1995)
15. Gardel, M.L., Shin, J.H., MacKintosh, F.C., Mahadevan, L., Matsudaira, P., Weitz , D.A.: Elastic behavior of cross-linked and bundled actin networks. Science **304**, 1301–1305 (2004)
16. Head, D., Levine, A., MacKintosh, F.: Deformation of cross-linked semiflexible polymer networks. Phys. Rev. Lett. **91**(10) (2003)
17. Head, D., Levine, A., MacKintosh, F.: Distinct regimes of elastic respone and deformation modes of cross-linked cytoskeletal and semiflexible polymer networks. Phys. Rev. E **68**, 061,907 (2003)
18. Huisman, E.M., van Dillen, T., Onck, P.R., der Giessen, E.V.: Three-dimensional cross-linked f-actin networks: relation between network architecture and mechanical behavior. Phys. Rev. Lett. **99** (2007)
19. Ingber, D.: Cellular tensegrity: defining new rules of biological design that govern the cytoskeleton. J. Cell Sci. **104**, 613–627 (1993)
20. Isambert, H., Maggs, A.C.: Dynamics and rheology of actin solutions. Macromolecules **29**, 1036–1040 (1996)
21. Janmey, P.A., Tang, J.X., Schmidt, C.F.: Actin filaments (unpublished)
22. Jordan, R., Kinderlehrer, D., Otto, F.: The variational formulation of the Fokker–Planck equation. SIAM J. Math. Anal. **29**, 1–17 (1999)
23. Kamm, R.D., Mofrad, M.R.K.: Cytoskeletal Mechanics: Models and Measurements. Cambridge University Press, Cambridge (2006)
24. Keller, H., Eggli, P.: Protrusive activity, cytoplasmic compartmentalization, and restriction rings in locomoting blebbing walker carcinosarcoma cells are related to detachment of cortical actin from the plasma membrane. Cell Motil. Cytoskeleton **41**(2), 181–193 (1998)
25. Kwon, R.Y., Lew, A.J., Jacobs, C.R.: A microsturcturally informed model for the mechanical response of three-dimensional actin networks. Comp. Methods Biomech. Biomed. Eng. **11**(4), 407–418 (2008)
26. Li, J., Dao, M., Lim, C.T., Suresh, S.: Spectrin-level modeling of the cytoskeleton and optical tweezers stretching of the erythrocyte. Biophys. J. **88**, 3707–3719 (2005)
27. Lions, J.L., Maday, Y., Turinici, G.: Resolution dedp par un schema en temps parareel. C. R. Acad. Sci. Paris **332**, 661–668 (2001)
28. Mitchison, T.J., Cramer, L.P.: Actin-based cell motolity and cell locomotion. Cell **84**, 371–379 (1996)
29. Mitran, S.: A time-parallel continuum–kinetic–molecular interaction algorithm for computation of nonequilibrium phenomena. J. Comput. Phys. (submitted) (2010)
30. Mofrad, M.R.K.: Rheology of the cytoskeleton. Ann. Rev. Fluid Mech. **41**, 433–453 (2009)
31. Palmer, J., Boyce, M.: Constitutive modeling of the stress strain behavior of f-actin filament networks. Acta Biomater. **4**(3), 597–612 (2008)
32. Pivkin, I., Karniadakis, G.: Accurate coarse-grained modeling of red blood cells. Phys. Rev. Lett. **101**(1), 118,105 (2008)
33. Pullarkat, P.A.: Loss of cell–substrate adhesion leads to periodic shape oscillations in fibroblasts. eprint arXiv:physics/0612156 (2006)
34. Ramaekers, F.C., Bosman, F.T.: The cytoskeleton and disease. J. Pathol. **204**, 351–354 (2004)
35. Rand, R.P., Burton, A.C.: Mechanical properties of the red cell membrane. i. Membrane stiffness and intracellular pressure. Biophys. J. **4**(2), 115–135 (1964)
36. Riskin, H.: The Fokker–Planck Equation. Springer, Heidelberg (1989)
37. Rottner, K., Lommel, S., Wehland, J., Stradal, T.: Pathogen-induced actin filament rearrangement in infectious diseases. J. Pathol. **204**, 396–406 (2004)

38. Seifert, U.: Modeling nonlinear red cell elasticity. Biophys. J. **75**(3), 1141–1142 (1998)
39. Sheetz, M.P., Sable, J.E., Döbereiner, H.: Continuous membrane–cytoskeleton adhesion requires continuous accommodation to lipid and cytoskeleton dynamics. Annu. Rev. Biophys. Biomol. Struct. **35**, 417–434 (2006)
40. Stamenovic, D., Coughlin, M.: A quantitative model of cellular elasticity based on tensegrity. J. Biomech. Eng. **122**(1), 39–43 (2000)
41. Takagi, Y., Homsher, E., Goldman, Y., Shuman, H.: Force generation in single conventional actomyosin complexes under high dynamic load. Biophys. J. **90**, 1295–1307 (2006)
42. Villani, C.: Optimal Transport: Old and New. Springer, Heidelberg (2009)
43. Wilhelm, J., Frey, E.: Elasticity of stiff polymer networks. Phys. Rev. Lett. **91**(10) (2003)